MDPI

*Article*

# Facile Adjustment of Exposed Crystal Facet of Hematite Derived-From Goethite to Enhance Cr (VI) Sorption

**Yuxin Li [1], Guocheng Lv [1],\*, Limei Wu [2], Zhaohui Li [3] and Libing Liao [1],\***

[1] Engineering Research Center of Ministry of Education for Geological Carbon Storage and Low Carbon Utilization of Resources, Beijing Key Laboratory of Materials Utilization of Nonmetallic Minerals and Solid Wastes, National Laboratory of Mineral Materials, School of Materials Science and Technology, China University of Geosciences (Beijing), Beijing 100083, China

[2] School of Materials Science and Engineering, Shenyang Jianzhu University, Shenyang 110168, China

[3] Geosciences Department, University of Wisconsin-Parkside, Kenosha, WI 53144, USA

\* Correspondence: guochenglv@cugb.edu.cn (G.L.); clayl@cugb.edu.cn (L.L.)

**Abstract:** The (110) facets of hematite have excellent adsorption performance for chromium. We aim to obtain hematite with a large specific surface area and exposed (110) facets by using natural needle-like goethite as the precursor. The derived hematite shows a significant increment in the removal capacity of chromium by six times compared with goethite under the same experimental conditions. Structural model fitting of extended X-ray absorption fine structure (EXAFS) spectroscopy suggested that the interatomic distance of Cr-Fe was approximately 3.6 Å for the Cr (VI) coordinated hematite with exposed (110) facets, which was characteristic of the form of bidentate binuclear surface complex. Molecular dynamic simulations for the arrangement of Cr (VI) in (110) facets of goethite and hematite indicated the superiority of hematite adsorption for chromium. We optimized efficient and economic permeable reactive barrier (PRB) materials by crystal plane adjustment based on these experimental and theoretical results. It was found that the life span of the column even reached 610 PVs when the initial concentration of Cr (VI) was 20 mg/L, which indicates its potential application in the field of PRB medium material.

**Keywords:** hematite; goethite; (110) facet; PRB; adsorption; Cr (VI)

## 1. Introduction

Hexavalent chromium, Cr (VI), is a common groundwater contaminant [1,2]. Long-term exposure to Cr (VI) will significantly impact human health and can even cause cancer and distortion [3]. Chromium exists in two stable forms of Cr (III) and Cr (VI) in natural water. Chromium's toxicity, stability, and solubility depend on its oxidation state. Cr (VI) has higher solubility and toxicity than Cr (III), and Cr (III) can be complexed by organic acid to be made bioavailable [4]. In soil environments, Cr (VI)'s mobility, reactivity, and bioavailability depend on adsorption reactions on iron oxide minerals [5,6]. Due to their superior adsorption performance, abundant reserves, and environmentally benign nature, iron oxides attract intensive attention [7,8]. Chromate exists in the form of anions in water and is usually combined with a positively charged adsorbent on the surface, especially iron oxides like hematite [9].

Natural hematite from different origins or synthesized by various methods has different exposed crystal facets and mainly expose (101), (112), (110), and (104) facets [10,11]. Hematite is usually facet-dependent for removing pollutants [12,13]. Different distributions of hydroxyl sites vary from every crystallographic facet, so there are wide variations in adsorption capacities for pollutants caused by the facet differentiation [14–17]. Based on the above research, the adsorbent can have higher adsorption performance by adjusting different exposed crystal facets [14,18]. Huang et al. used different synthesis methods to prepare hematite with different exposed crystal facets. They found that the adsorption

of Cr (VI) on (110) facets of hematite was higher than that on (001) facets [19]. In recent years, more porous minerals with the micro-/meso-porous structure have been used to remove pollutants, such as Cr (VI), from aqueous because of their high specific surface area (SSA) [20,21]. Permeable reactive barrier (PRB), an in situ remediation technology, uses porous materials as a medium to remove contaminants from groundwater [22,23]. Various calcined-based adsorbents with chemical stability are used because of their large ionic exchange capacity and low density, especially porosity [24,25]. It has been found that porous hematite has a better removal effect on As (V), which was prepared by calcinating natural siderite and goethite [26]. Previous studies have shown that naturally occurring iron (hydrogen) oxides may have better reactivity than synthetic ones [27]. Calcinating pristine goethite at different temperatures will produce many internal pores and become hematite after dehydration, which significantly improves its surface area [28].

In this paper, hematite with larger internal pores was prepared by calcining the precursor—natural goethite—and the produced hematite had higher exposure to specific crystal facets (110). The pristine mineral and calcined products were characterized by XRD (X-ray diffraction), HRTEM (High-resolution transmission electron microscopy), FTIR (Fourier transform infrared spectrometer), and BET (Brunauer–Emmet–Teller) to ascertain the effect and rules of calcining temperature on its morphology and phase transformation. The adsorption process was studied by equilibrium and kinetic adsorption experiments. According to the results of static adsorption, the hematite (goethite calcined at 350 °C for 1 h) was used for the first time as the filler of a PRB column, and the service life of the barrier was estimated.

## 2. Materials and Methods

The natural goethite and hematite were collected from Chenzhou, Hunan Province, in southern China. The crude ore was crushed and sieved through a 200-mesh sieve. After sieving, the high-purity goethite powder was calcined at 25, 150, 250, 350, 450, and 550 °C in a muffle furnace at a heating rate of 5 °C/min for 1 h. A 2.8287 g aliquot of $K_2Cr_2O_7$ was dissolved in 1 L of deionized (DI) water to prepare a stock solution of Cr (VI).

### 2.1. Characterizations

XRD was conducted on an X-ray powder diffractometer (D8 Advance, Bruker, Germany) with Cu K$\alpha_1$ ($\lambda$ = 1.5406 Å) radiation at 40 kV and 100 mA, a scanning speed of 8° $2\theta$/min, and a step size of 0.02° $2\theta$ from 5° to 90°. The samples were evenly mixed with the KBr at a mass ratio of 1:40, and then were scanned by FTIR spectrophotometer (Spectrum 100, PerkinElmer, Waltham, MA, USA) to obtain the FTIR spectra. X-Ray Fluorescence Spectrometer (XRF, Thermo electron corporation, ARLADVANT X, MA, USA) was used to confirm the chemical composition of the sample with K$\alpha$ spectra of the elements. Additionally, the morphologies of the samples were observed by HRTEM (JEM-2100, JEOL, Tokyo, Japan), and the BET specific surface area was determined from $N_2$ adsorption–desorption isotherms by an automated gas sorption instrument (Micro Active for ASAP 2460, Atlanta, USA). The UV-Vis spectrophotometer (Shanghai, Precision Scientific Instrument Co., Ltd., Shanghai, China) was used to detect the removal amount of Cr (VI).

### 2.2. Removal of Cr (VI)

The batch experiments of removal of Cr (VI) on goethite and its calcined products were carried out by changing the initial concentration and contact time while the adsorbent dosage was fixed at 5 g/L. Standard solutions with different concentrations of 5, 10, 20, 50, 75, 100, 150, and 200 mg/L were obtained by diluting the stock solution, and a volume of 20 mL Cr (VI) solution was used in all batch experiments, and the pH of the solution was adjusted to neutral with 0.1 M KOH and 0.1 M HCl. After a day of shaking on a reciprocal shaker at 150 rpm, the mixture was centrifuged at 8000× *g* rpm for another 10 min. Using a reciprocal shaker to shake the mixture for 0.1, 0.25, 0.5, 1, 2, 4, 8, 12, and 16 h with the initial concentration of 200 mg/L, the equilibrium Cr (VI) concentrations were determined

by testing the suspensions. The 1, 5-diphenylcarbazide method was used to figure out the residual Cr (VI) concentration of the solution by UV-vis spectrophotometer in glass cuvettes with 10 mm optical path at a wavelength of 540 nm [29].

### 2.3. Transport of Cr (VI)

The calcined material hematite (20~50 mesh) was then packed into glassy columns to simulate a PRB reaction column (Figure S1). The columns were 3.6 cm in diameter and 15 cm in total height, filled with quartz sand, hematite, and quartz sand from bottom to top (the particle size of quartz sand is 2~3 mesh). The filling height of each medium material was 5 cm, and the total weight of the hematite was 102 g per column. The columns were fed with DI water until they were fully saturated. The volumes of hematite and pore could be calculated, respectively, from the weight difference before and after immersion, and the bulk density of the hematite was 2.01 g/cm$^3$. The ratio of the volume of water under saturated conditions to hematite determined that the porosity of the packed columns was 0.59. The groundwater flow rate was simulated according to the porosity of the hematite, and the flow rate was set at 0.42 mL/min. Cr (VI) aqueous solutions with concentrations of 5 mg/L and 20 mg/L of simulated pollutants were fed into the two experimental columns, respectively, in an upward direction using a 2-head peristaltic pump in an upward direction, and the Darcy flux was 4.17 cm/h. The effluents were taken and measured for the adsorption concentration every 8 h. Then, the solution was switched to DI water and fed it for desorption when a breakthrough happened in experimental columns. The hematite had good hydraulic properties, which can be seen from the hydraulic conductivity (3.46 cm/h) of the hematite, indicating that the hematite was feasible as a permeable reactive barrier material.

### 2.4. Cr K-Edge EXAFS Spectroscopy

SPring-8 (Super Photon ring-8) at JASRI (Japan Synchrotron Radiation Research Institute) was applied to measure the Cr K-edge EXAFS spectroscopy of hematite after the adsorption reaction. The calibrated Si (111) double crystal monochromator was used to scan the incident X-ray energy across the Cr K-edge EXAFS region. The electron energy was about 8.0 GeV, and the current was about 99.5 mA in the storage ring. In the transmission mode, the compound $K_2Cr_2O_7$ was detected as a reference, and the sample after the adsorption reaction was measured in the fluorescence mode in the case of a relatively low Cr concentration. R-space was originated in EXAFS data by performing Fourier transform on the $\chi(k)$ function. Details of data acquisition are provided in Supplementary Materials Text S1. The data were manipulated by making use of the program Artemis to fit all data sets in R-space [30]. The fitting was performed to optimize the coordination number (*CN*) and the distance (*R*) as well as the disorder factor($\sigma^2$). The first shell (Cr-O) fit was the basis of the energy shift value, and higher shell fitting was acquired by fixing at these values. The FEFF model was utilized to clarify the phase and amplitude functions of the adsorber and backscatters [31]. The same parameters were applied to model the spectrum after back-transforming and fitting every single peak in the Fourier transform spectra.

### 2.5. Methods of Molecular Simulation

The sorption sites of Cr (VI) on goethite and hematite were investigated by molecular simulation in the module Forcite of Materials Studio 7.1 [32]. The parameters *a* = 4.598 Å, *b* = 9.951 Å, *c* = 3.018 Å, and $\alpha = \beta = \gamma = 90°$ for goethite and *a* = 5.028 Å, *b* = 5.028 Å, *c* = 13.736 Å, and $\alpha = \beta = 90°$, $\gamma = 120°$ for hematite were applied to describe the resulting primitive unit cell, and it was the basis of building a series of ($3 \times 2 \times 1$) supercells. The Generalized Gradient Approximation (GGA) was used to optimize the primitive unit cells of these two minerals for the exchange-correlation potential (PW91). It was applicable for relatively weak interactions in the model. Periodic boundary conditions, k-point, and plane wave basis set were applied by CASTEP, and ultrasoft pseudopotentials were adopted. The energy cutoff was 300 eV for the plane wave expansion, and just one special k-point situated

at (0.00, 0.00, 0.00) was permitted in the Brillouin zone. The later analyses were based on the data collected on the last 200 ps when the time was 1 ns and the setting of the time step was 1 fs at the temperature of 298 K. Density functional theory–Dispersion (DFT-D2)-correction was employed to obtain all the GGA-PW91 calculations. More explanation of these terms is provided in Text S2 [33].

*2.6. Simulation of Cr (VI) Transport*

HYDRUS-1D (version 4.16) was employed to simulate the experimental column data. The one-dimensional transport behavior of solutes in porous media was described as sequential first-order decay and reversible sorption by the partial differential equation in the former study [34].

### 3. Results and Discussion

*3.1. Characterization of Goethite and Calcined Product*

The XRD patterns of goethite and its calcined products are shown in Figure 1. All peaks of the pristine mineral were identified as goethite with no impurities by comparing with the standard pattern (JCPDS No. 8-97), which was consistent with the XRF results (Table S1, Supplementary Materials) showing that the content of iron oxides existed in the form of goethite was as high as 95.95%. When the calcination temperature was varied from 350 to 550 °C, the peaks of goethite disappeared, and new characteristic peaks appeared, which were identified as hematite. The intensity of the peak increased with increasing temperature. According to the peak intensity of the standard diffraction pattern JCPDS No. 1-1053, it indicated that after calcination at a temperature above 350 °C, the obtained hematite had a preferred development of (110) facets indicated by a sharp diffraction peak, which could be seen in the pink area in Figure 1. This was also consistent with the exposed crystal facet in the literature [19]. The grain size determined from the (110) facet was much larger than that from the other facets by calculating with the Scherrer formula (Table S2) [35]. This indicated that perhaps the hematite formed after calcination exposes the (110) facet. In addition, the diffraction peak intensity of this facet gradually increased when we prolonged the calcination time, and the hematite crystal grains grew along the *c*-axis (Figure S2, Supplementary Materials).
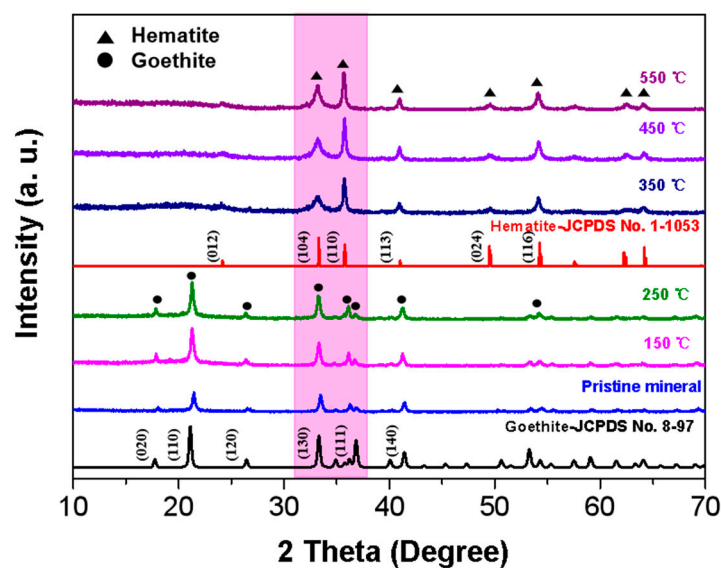


**Figure 1.** XRD patterns of goethite and calcined goethite at different temperatures.

In order to explore the change of functional groups with calcination temperature, the technique of FTIR was utilized. The FTIR spectra of different samples were shown in Figure 2. The goethite at 25 °C showed that the stretching of OH- could cause a broad band

at 3112 cm$^{-1}$ [36]. A distinct absorption band at 1650 cm$^{-1}$ was caused by $H_2O$ [37]. The bands at 894 and 799 cm$^{-1}$ were due to bending vibrations of Fe-O-H in goethite [38]. The band at 460 cm$^{-1}$ was due to symmetric Fe-O stretching vibration. When the goethite was calcined, hydroxyl groups coordinated with iron atoms on the surface, and a new band at 3380 cm$^{-1}$ developed, which was attributed to the OH-stretching, and the position of $H_2O$-band would shift to 1630 cm$^{-1}$ [39]. A set of new bands at 519.0 and 431.6 cm$^{-1}$ appeared and represented characteristics of hematite [40].
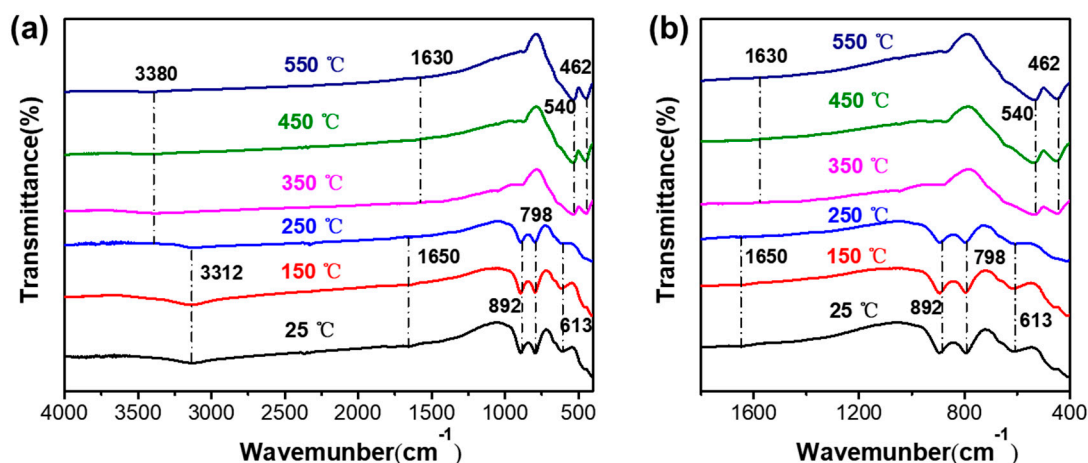


**Figure 2.** The FT-IR spectroscopy of pristine goethite and the calcined products of goethite at different temperatures for 1 h. (**a**) all spectrum, (**b**) regions of 1800-450 cm$^{-1}$.

The TEM images in Figure 3 showed the morphology of pristine goethite (a, b, c) and hematite at 350 °C (d, e, f), respectively. The images revealed that goethite is rod-like, acicular, and bulky in nature [28]. The lattice fringes of 0.421 nm in the image (Figure 3c) were consistent with the (110) facet of goethite [41], while the lattice fringes of calcined goethite (0.252 nm) in Figure 3f were consistent with the (110) facet of hematite [42]. It can be observed that the external appearances of the calcined samples are retained from natural goethite in Figure 3d. This also supported the conclusion that calcining goethite at high temperatures could make the produced hematite preferentially oriented and control its exposure to a specific crystal plane (110). Furthermore, plenty of slit-like micropores were parallel to the elongated direction of the hematite microcrystal. Obviously, this was caused by the dehydroxylation of goethite.
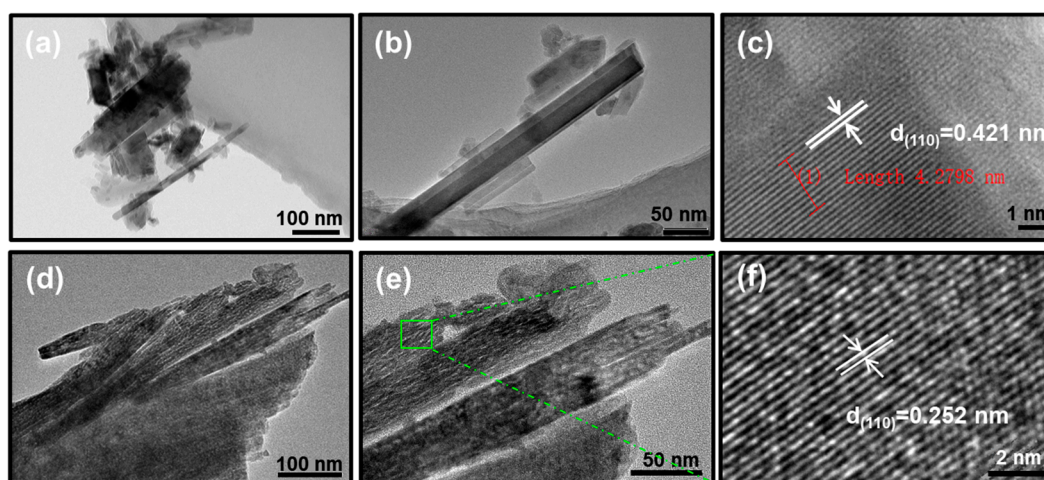


**Figure 3.** The HRTEM image of pristine goethite (**a–c**) and calcined product prepared at 350 °C for 1 h (**d–f**). The green square area is enlarged as Figure 3f.

To determine the BET surface area, the $N_2$ adsorption/desorption isotherms were tested, and the results are given in Figure S3. The adsorption/desorption isotherms of goethite and hematite belonged to the type-II category according to the IUPAC classification, which means the meso-porosity is due to capillary condensation [43]. The hysteresis loop of goethite could be classified as $H_2$-type, and the desorption line dropped sharply at medium relative pressure. The corresponding hole for this type of hysteresis loop was a slit composed of parallel plates that were close together. At high $p/p_0$, the hysteresis ring shape of the calcined goethite did not exhibit any limiting adsorption and was classified as $H_3$-type. This type of isotherm was caused by the aggregation of plate-like particles into pores [44]. This also supported the TEM image above, which showed that long and narrow pores were produced by massive goethite after calcination.

The Brunauer-Emmett-Teller (BET) surface area of goethite was 36.6 $m^2/g$. After calcination at 350 °C, the surface area increased to the maximum of 124.4 $m^2/g$, and then the surface area reduced rapidly with the increasing temperature beyond 350 °C. Meanwhile, the total pore volume reached its maximum value at 350 °C. The pore volume of goethite at 25 °C was 0.033 $cm^3/g$ and increased to the maximum of 0.216 $cm^3/g$ at 350 °C (Liu et al., 2013). Liu et al. pointed out that with the increase in calcination temperature, the hydroxyl group of goethite would be gradually removed, which resulted in the specific surface area having a significant increase at 350 °C. Then, there was a decrease when heating goethite above 350 °C due to grain coarsening. Hence, it can be seen that hematite calcined at 350 °C had the maximum number of active surface sites from the results of surface area and pore volume (Table 1). The insertion in Figure S3 exhibited the Barrett-Joyner-Halenda (BJH) pore size distribution curve of the samples. The pore size reached 8.3 nm at 350 °C and decreased sharply to 1.8 nm when the temperature reached 450 °C, and then there was no significant change as the temperature went up. The pore size showed that the adsorbents were mesoporous in nature. In addition, these findings coincided with the TEM analysis results. When the calcination temperature of goethite reached 350 °C, the phase would turn into hematite and produce a large number of nano-scale slits inside. This also exposed the (110) facets, which were favorable for adsorption performance.

**Table 1.** BET surface area and pore characteristics of goethite and its calcined products at different temperatures.

| Sample | | 25 °C | 150 °C | 250 °C | 350 °C | 450 °C | 550 °C |
|---|---|---|---|---|---|---|---|
| Surface Area | ($m^2/g$) | 36.6 | 81.2 | 92.6 | 124.4 | 115.0 | 114.0 |
| Pore Volume | ($cm^3/g$) | 0.033 | 0.086 | 0.129 | 0.216 | 0.060 | 0.065 |
| Pore Size | (nm) | 1.8 | 2.4 | 5.0 | 8.3 | 3.5 | 3.0 |

### 3.2. Adsorption Isotherm

The adsorption capacity and affinity of adsorbent can be obtained using adsorption isotherms. The isotherm study was used to determine the amount of pollutant adsorbed per unit of adsorbent and remaining in the solution at equilibrium. The data obtained from the batch experiment were analyzed using isotherm models such as Langmuir [45–47] and Freundlich [48,49] (Text S3, Supplementary Materials). Table S3 shows that the adsorption behavior of Cr (VI) onto hematite was not a multi-molecular adsorption process. According to Table S4 [39,50,51], the conclusion that goethite and hematite had poor adsorption performance could be drawn. To compare the removal ability of Cr (VI), the hematite derived from goethite, the hematite ore (collected from Chenzhou, Hunan Province, XRD pattern was shown in Figure S4a), and goethite ore were used to remove Cr (VI). The adsorption capacity of Cr (VI) onto the hematite derived from goethite was 2.95 mg/g (Figure 4a) under the condition of pH 7 in this paper, which was about six times that of goethite (0.49 mg/g) and 3.4 times of hematite ore (0.86 mg/g) (Figure S4b). The pH value exerted a tremendous influence on chromium adsorption, and the adsorption of $HCrO_4^-$ onto hematite under acidic conditions was much stronger than that of $CrO_4^{2-}$ at neutral

pH [19,52]. The result showed that hematite had a higher adsorption capacity than other sorbents listed in the table.
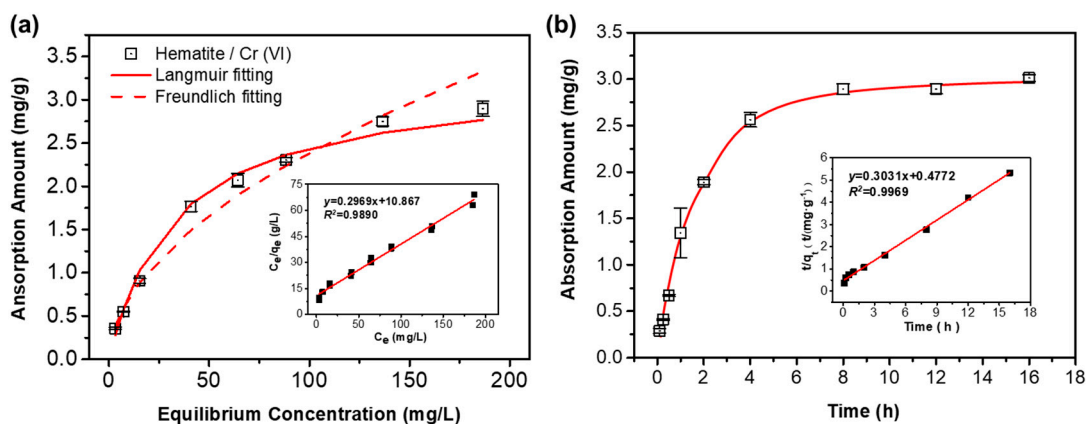


**Figure 4.** Cr (VI) adsorption by hematite. The data were fitted to the Freundlich (dashed line) and Langmuir (solid line) isotherm models. The insert is Langmuir adsorption isotherms (**a**); Kinetics of Cr (VI) adsorption by hematite fitted to the pseudo-second-order kinetics (solid line). The insert is the linear plot of the pseudo-second-order reaction (**b**).

### 3.3. Adsorption Kinetics

In the research field of solid–liquid adsorption, the more widely used kinetic adsorption models are the pseudo-first-order kinetic model [53] and the pseudo-second-order kinetic model [54] (Text S4, Supplementary Materials). The adsorption data of hematite (calcined at 350 °C) were fitted by these two dynamics models as described above (Figure 4b). Compared with the calculated equilibrium capacity of both kinetic models, the value of the pseudo-second-order model (3.0 mg/g) was closer to the experimental equilibrium capacity. The adsorption equilibrium was reached after 8 h. The pseudo-second-order kinetic model showed an excellent linear correlation with an $R^2$ value of 0.9969 (Table S5). Therefore, the adsorption of Cr (VI) onto hematite could be described in pseudo-second-order kinetics.

### 3.4. The Local Coordination Environment

The adsorption mechanism of Cr by hematite can be determined by the Cr (VI)/hematite coordination environment, which can be conducted by Cr *K*-edge EXAFS spectroscopy measurements. A coordination environment of Cr (VI)/hematite was determined by Cr *K*-edge EXAFS spectroscopy measurements. Fourier transformation of the $\chi(k)$ function created a radial structure-function, and the information of interatomic distance within the material could come from the corresponding peak position. Since there was no correction for the phase shifts, there was a slight deviation from the actual interatomic distances (Figure 5a). The experimental spectra and the parameters ($R$, $CN$, and $\sigma^2$) could be fitted to a theoretical model by back-transforming the spectra based on the optimized fit and the parameters, and the R factors (goodness of fit) of the local coordination environment for Cr (VI) adsorption on hematite are shown in Table S6. The local coordination environment was confirmed by fitting the Fourier filtered $\chi(k)$ function (0~4 Å) (Figure 5b). In the Fourier transform curve, the fitting results for the first peak were consistent with the experimental data with an average distance (1.65 Å) of four oxygen atoms to the central Cr atom. Compared with the Cr-O bond ($R_{\text{Cr-O}}$) length of the tetrahedral species ($HCrO_4^-$) in previous reports, this average bond length of $R_{\text{Cr-O}}$ matched very well [55,56]. The distance of 2.7 Å is accounted for by Cr-O-O double-scattering [57]. $CN_{\text{Cr-Fe}}$ was found to be 0.6, and $R_{\text{Cr-Fe}}$ was approximately 3.36 Å for Cr (VI) adsorption, which accorded with previous studies on the adsorption of Cr (VI) onto hematite [17]. The average interatomic distance of Cr-Fe was 3.36 Å, which was consistent with the Cr-Fe distance of the Cr (VI) complexes in the form of bidentate binuclear. Different complexation reactions could take place on different crystal facets of hematite independently. Hence, Cr (VI) was complexed on the

(110) facets of hematite in the form of bidentate binuclear according to the existence of average Cr-Fe interatomic distances.
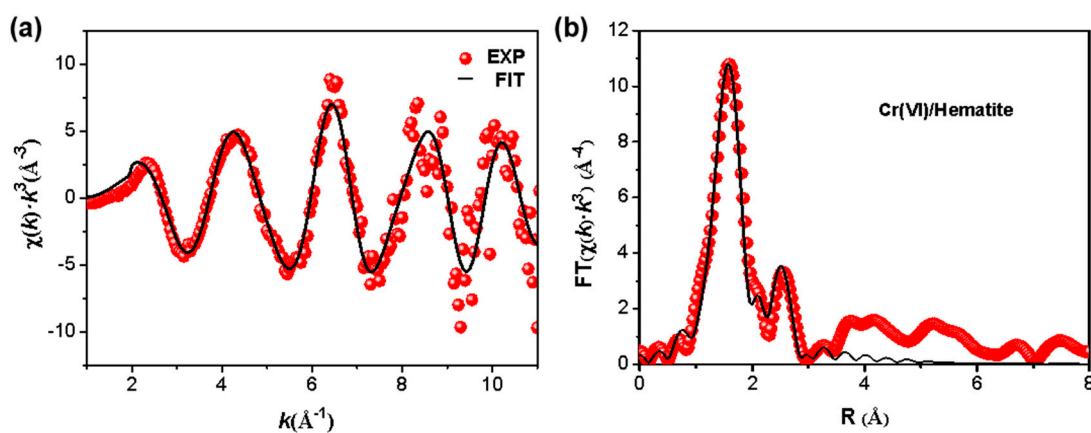


**Figure 5.** The $k^3$-weighted K-edge EXAFS spectra (**a**) of Cr (VI) on hematite show the fit (solid black line) of the theoretical curve to the experimental curve (red spheres). Fourier-transformed spectra (**b**) of Cr (VI) adsorbed on hematite resulting in a radial structure-function. The peak positions correspond to the distances of the atomic shells but are uncorrected for phase shifts.

### 3.5. Molecular Simulation

The radial distribution of Cr and Fe can be simulated with software. The study of the arrangement of Cr, goethite, and hematite was based on Fe representing iron (hydr)oxide and Cr (central positive group in $K_2Cr_2O_7$) representing $K_2Cr_2O_7$, with the results shown in Figure 6c,d. Initially, goethite was located at 22~37.5 Å, while arrangements of Cr stayed at 3.5~8 Å and 9~10.3 Å. Hematite was located at 21.7~38 Å, while arrangements of Cr stayed at 11~14.2 Å and 15.3~18 Å. When goethite was calcined, the distance between chromium and goethite was longer than between chromium and hematite. This means the phase transition resulting from calcination strongly affects locations of Cr and thermal modification renders a shorter distance of Cr to hematite, indicating stronger interaction.
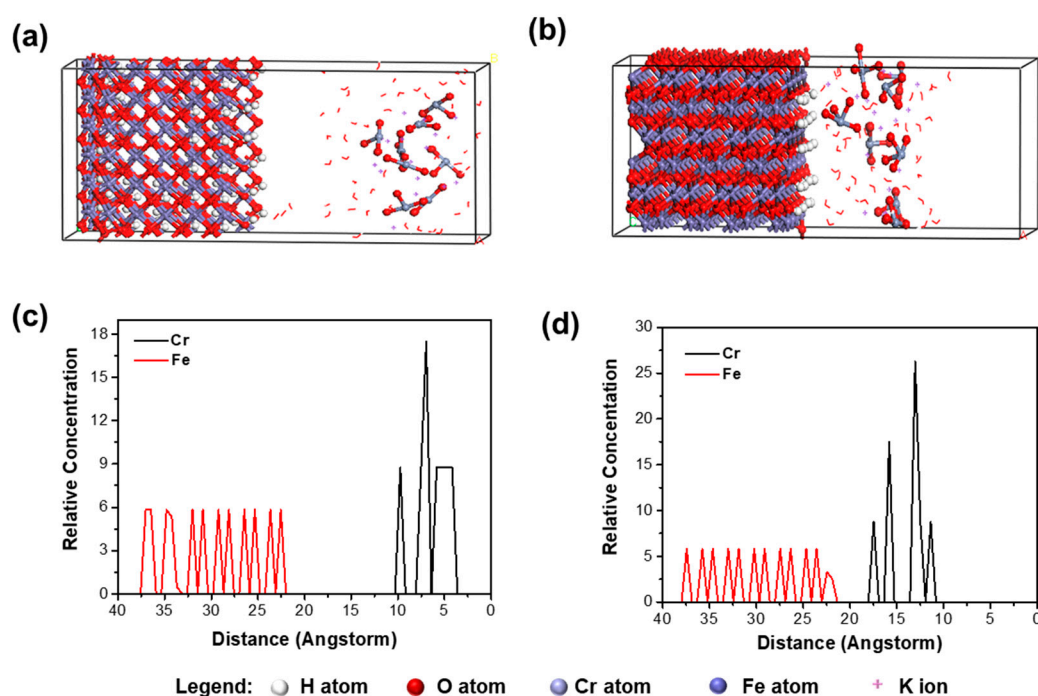


**Figure 6.** Fitting of Cr adsorption on (110) plane of goethite (**a**) and hematite (**b**); the distribution of Fe/Cr on (110) plane of goethite (**c**) and hematite (**d**).

*3.6. Column Transport of Cr (VI)*

Chromium removal has been studied by column experiments in many pieces of literature [58,59]. The ratio of the treated water volume to the pore volume (PV) of the packed material is defined as the life span of the column. When the pollutant concentration of the effluent is half of the input concentration, the ratio of the number of PVs is used to evaluate the performance of the column [60,61]. The PVs value of the goethite column was 7, indicating only negligible sorption of Cr (VI) (Figure S5), and there was no Cr (VI) reduction according to the concentration at the complete breakthrough, which was almost the same as the input concentration.

The Cr (VI) solute transport behavior and breakthrough curves were shown in Figure 7a,b. At an initial concentration of 5 mg/L and 20 mg/L, the columns reached saturation after continuous operation for 552 h and 502 h, respectively. When $C_t/C_0 = 0.5$, the number of PVs was about 871 for a column with an initial concentration of 5 mg/L and 610 PVs for 20 mg/L. The HYDRUS-1D solute transport model was used to fit the Cr (VI) transport results through hematite columns under different conditions. The hematite had a dispersion of 23 cm under the initial concentration of 5 mg/L and a dispersion of 2.6 cm under the input concentration of 20 mg/L, and the coefficient of determination $R^2$ was 0.95 and 0.99, respectively, when the experimental data were fitted by the software HYDRUS-1D (Table 2). Compared with the higher adsorption capacity in the batch experiment, the adsorption capacity in the column experiment at different input concentrations was 2.67 and 1.3 mg/g, respectively. There were two main reasons for the smaller adsorption capacity of the column experiment.
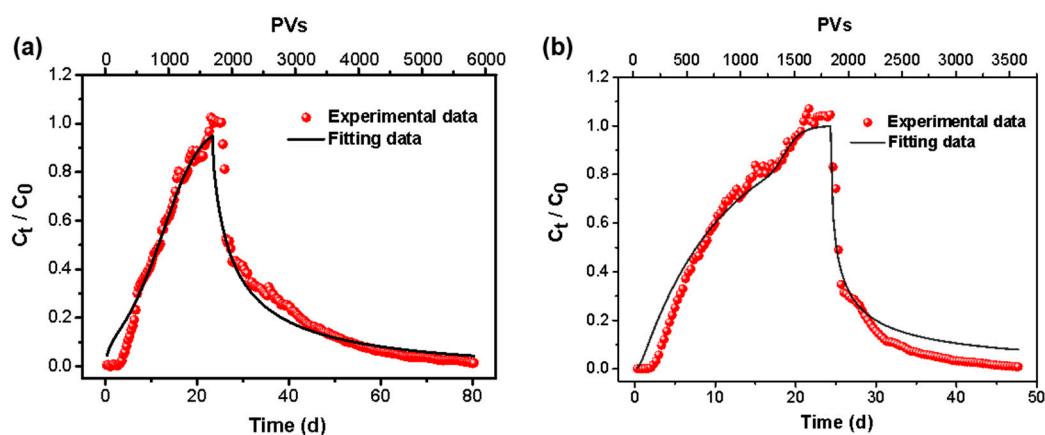


**Figure 7.** The breakthrough curve of Cr (VI) in different concentrations (**a**) 5 mg/L and (**b**) 20 mg/L for a column packed with hematite.

**Table 2.** Parameter values obtained from HYDRUS-1D for Cr (VI) transport through columns packed with hematite in different concentrations.

| Column | $\alpha_L$ [a] | $K$ [b] | $H$ [c] | $S_m$ [d] | $C_0$ | $\mu_L$ [e] | $R^2$ |
|---|---|---|---|---|---|---|---|
| | (cm) | (L/g) | (L/g) | (mg/g) | (mg/L) | (h$^{-1}$) | |
| Hematite | 23 | 373 | 0.151 | 2.67 | 5 | 0.0018 | 0.9472 |
| Hematite | 2.6 | 1622 | 0.122 | 1.30 | 20 | 0.0020 | 0.9894 |
| Batch | | | 0.2 | 2.95 | | | |

[a] Denotes dispersity; [b] denotes empirical coefficients; [c] denotes treatment efficiency; [d] denotes sorption amount; [e] denotes first-order decay constant.

On the one hand, hematite with a larger size was used in the column experiment to avoid column blockage, which also reduced its specific surface area. On the other hand, the hydraulic retention time in the column experiment was too short to react adequately between Cr (VI) and hematite. However, the solute transport in column experiments was

more similar to practical engineering applications than batch experiments if the hematite was used as packing materials in PRB.

## 4. Conclusions

Goethite and hematite are common iron oxides in the earth's crust, and these minerals greatly influence the mobility and transport of chromium in the crust. Many researchers have studied the surface adsorption of different crystal facets of hematite and the internal adsorption mechanism from the molecular level and confirmed that the hematite (110) facets have a high adsorption capacity for Cr (VI). Goethite naturally has a needle-like morphology and exposes (110) crystal planes. This study used the characteristics of goethite to obtain hematite that inherits its morphology through simple calcination, thereby realizing the control of exposed specific facets of hematite. The adsorption performance of hematite was greatly improved, and the Cr (VI) was complexed on the surface of hematite in bidentate and binuclear. Hematite was used as a PRB reactive media material, and it was found that the PVs of the column even reached 610 when the initial concentration of Cr (VI) was 20 mg/L. The saturated adsorption time was significantly prolonged compared to the goethite column. As far as we know, this is the first time that hematite with exposed (110) facets has been prepared using goethite as a precursor, and it is the first time that hematite with exposed specific facets has been used as a PRB medium material to remove Cr (VI) from groundwater. It is confirmed that hematite has excellent prospects in the remediation of chromium-containing wastewater in situ and provides an approach for the green utilization of iron oxide minerals.

**Supplementary Materials:** The following supporting information can be downloaded at: https://www.mdpi.com/article/10.3390/cryst13010079/s1. Additional texts, figures, and tables as mentioned in the text (PDF). Text S1: EXAFS study; Text S2: Molecular Simulation; Text S3: Adsorption isotherms; Text S4: Adsorption kinetics; Figure S1: Schematic of the experimental column; Figure S2: X-ray diffraction patterns; Figure S3: $N_2$ adsorption-desorption isotherms; Figure S4: Cr (VI) adsorption by three materials; Figure S5: Breakthrough curve of Cr (VI); Table S1: X-Ray Fluorescence results of pristine goethite; Table S2: Grain size of calcined goethite; Table S3: Comparison of isotherm models of Cr (VI) adsorption by hematite; Table S4: Comparison of adsorption properties; Table S5: Comparison of kinetic parameters; Table S6: Parameters of EXAFS spectroscopy.

**Author Contributions:** Y.L.: Data collection and analysis, Investigation, Writing-original draft preparation; G.L.: Supervision, Writing-Reviewing and Editing; L.W.: Software; Z.L.: Drafting; L.L.: Writing—Review and Editing. All authors have read and agreed to the published version of the manuscript.

**Conflicts of Interest:** The authors declare that they have no known competing financial interests or personal relationships that could have appeared to influence the work reported in this paper.

## References

1. Mekatel, H.; Amokrane, S.; Bellal, B.; Trari, M.; Nibou, D. Photocatalytic reduction of Cr (VI) on nanosized $Fe_2O_3$ supported on natural Algerian clay: Characteristics, kinetic and thermodynamic study. *Chem. Eng. J.* **2012**, *200*, 611–618. [CrossRef]
2. Chen, K.; Bocknek, L.; Manning, B. Oxidation of Cr (III) to Cr (VI) and production of Mn (II) by synthetic manganese (IV) oxide. *Crystals* **2021**, *11*, 443. [CrossRef]
3. Khan, T.; Isa, M.H.; Ul Mustafa, M.R.; Yeek-Chia, H.; Baloo, L.; Sabariah, B.A.M.; Teh Saeed, M.O. Cr (VI) adsorption from aqueous solution by an agricultural wastebased carbon. *RSC Adv.* **2016**, *6*, 56365–56374. [CrossRef]
4. O'Brien, P.; Kortenkamp, A. The chemistry underlying chromate toxicity. *Transition Met. Chem.* **1995**, *20*, 636–642. [CrossRef]
5. Johnston, C.P.; Chrysochoou, M. Investigation of chromate coordination on ferrihydrite by in Situ ATR-FTIR spectroscopy and theoretical frequency calculations. *Environ. Sci. Technol.* **2012**, *46*, 5851–5858. [CrossRef] [PubMed]

6. Yang, X.; Xia, L.; Li, J.; Dai, M.; Yang, G.; Song, S. Adsorption of As (III) on porous hematite synthesized from goethite concentrate. *Chemosphere* **2017**, *169*, 188–193. [CrossRef] [PubMed]

7. Mitar, I.; Guć, L.; Soldin, Ž. Rapid microwave method for synthesis of iron oxide particles under specific conditions. *Crystals* **2021**, *11*, 383. [CrossRef]

8. Chahal, S.; Kumar, A.; Kumar, P. Zn doped $\alpha$-Fe$_2$O$_3$: An efficient material for UV driven photocatalysis and electrical conductivity. *Crystals* **2020**, *10*, 273.

9. Fendorf, S.E. Surface reactions of chromium in soils and waters. *Geoderma* **1995**, *67*, 55–71. [CrossRef]

10. Jiang, S.; Yan, X.; Peacock, C.L.; Zhang, S.; Yin, H. Adsorption of Cr (VI) on Al-substituted hematite and its reduction and retention in the presence of Fe$^{2+}$ under conditions similar to subsurface soil environments. *J. Hazard. Mater.* **2020**, *390*, 122014. [CrossRef]

11. Huang, X.; Hou, X.; Song, F.; Zhao, J.; Zhang, L. Ascorbate induced facet dependent reductive dissolution of hematite nanocrystals. *J. Phys. Chem. C.* **2017**, *121*, 1113–1121. [CrossRef]

12. Huang, X.; Hou, X.; Zhang, X.; Rosso, K.; Zhang, L. Facet-dependent contaminant removal properties of hematite nanocrystals and their environmental implications. *Environ. Sci. Nano* **2018**, *5*, 1790–1806. [CrossRef]

13. Huang, J.; Jones, A.; Waite, T.; Chen, Y.; Huang, X.; Rosso, K.; Kappler, A.; Mansor, M.; Tratnyek, P.; Zhang, H. Fe (II) redox chemistry in the environment. *Chem. Rev.* **2021**, *121*, 8161–8233. [CrossRef]

14. Catalano, J.G.; Fenter, P.; Park, C. Water ordering and surface relaxations at the hematite (110)-water interface. *Geochim. Cosmochim. Acta.* **2009**, *73*, 2242–2251. [CrossRef]

15. Catalano, J.G. Weak interfacial water ordering on isostructural hematite and corundum (001) surfaces. *Geochim. Cosmochim. Acta.* **2011**, *75*, 2062–2071. [CrossRef]

16. Komárek, M.; Koretsky, C.M.; Stephen, K.J.; Alessi, D.S.; Chrastný, V. Competitive adsorption of Cd (II), Cr (VI), and Pb (II) onto nanomaghemite: A spectroscopic and modeling approach. *Environ. Sci. Technol.* **2015**, *49*, 12851–12859. [CrossRef] [PubMed]

17. Noerpel, M.R.; Sang, S.L.; Lenhart, J.J. X-ray analyses of lead adsorption on the (001), (110), and (012) hematite surfaces. *Environ. Sci. Technol.* **2016**, *50*, 12283–12291. [CrossRef] [PubMed]

18. Liang, Y.; Wang, M.; Xiong, J.; Hou, J.; Wang, X.; Tan, W. Al-substitution-induced defect sites enhance adsorption of Pb$^{2+}$ on hematite. *Environ. Sci.: Nano.* **2019**, *6*, 1323–1339. [CrossRef]

19. Huang, X.; Hou, X.; Song, F.; Zhao, J.; Zhang, L. Facet-dependent Cr (VI) adsorption of hematite nanocrystals. *Environ. Sci. Technol.* **2016**, *50*, 1964. [CrossRef]

20. Yan, L.; Yang, K.; Shan, R. Calcined ZnAl- and Fe$_3$O$_4$/ZnAl-layered double hydroxides for efficient removal of Cr (VI) from aqueous solution. *RSC Adv.* **2015**, *5*, 96495. [CrossRef]

21. Ai, L.; Huang, H.; Chen, Z.; Xing, W.; Jiang, J. Activated carbon/CoFe$_2$O$_4$ composites: Facile synthesis, magnetic performance and their potential application for the removal of malachite green from water. *Chem. Eng. J.* **2010**, *156*, 243–249. [CrossRef]

22. Obiri-Nyarko, F.; Grajales-Mesa, S.; Malina, G. An overview of permeable reactive barriers for in situ sustainable groundwater remediation. *Chemosphere* **2014**, *111*, 243–259. [CrossRef] [PubMed]

23. Faisal AA, H.; Sulaymon, A.H.; Khaliefa, Q.M. A review of permeable reactive barrier as passive sustainable technology for groundwater remediation. *Int. J. Environ. Sci. Technol.* **2017**, *4*, 1–16. [CrossRef]

24. Sungworawongpana, S.; Pengprecha, S. Calcination effect of diatomite to chromate adsorption. *Procedia. Eng.* **2011**, *8*, 53–57. [CrossRef]

25. Xu, Y.; Zhang, J.; Qian, G.; Ren, Z.; Xu, Z.P.; Wu, Y.; Liu, Q.; Qiao, S. Effective Cr (VI) removal from simulated groundwater through the hydrotalcite-derived adsorbent. *Ind. Eng. Chem. Res.* **2010**, *49*, 2752–2758. [CrossRef]

26. Dai, M.; Xia, L.; Song, S.; Peng, C.; Valdivieso, L. Adsorption of As (V) inside the pores of porous hematite in water. *J. Hazard. Mater.* **2016**, *307*, 312–317. [CrossRef]

27. Dorau, K.; Pohl, L.; Henke, C.; Hschen, C.; Mueller, C.W. Soil organic matter and phosphate sorption on natural and synthetic Fe oxides under in situ conditions. *Environ. Sci. Technol.* **2019**, *53*, 13081–13087. [CrossRef]

28. Liu, H.; Chen, T.; Zou, X.; Qing, C.; Frost, R.L. Thermal treatment of natural goethite: Thermal transformation and physical properties. *Thermochimica. Acta.* **2013**, *568*, 115–121. [CrossRef]

29. Bartlett, R.; James, B. Behavior of chromium in soils: III. Oxidation 1. *J. Environ. Qual.* **1979**, *8*, 31–35. [CrossRef]

30. Ravel, B.; Newville, M. Athena, artemis, hephaestus: Data analysis for X-ray absorption spectroscopy using IFEFFIT. *J. Synchrotron Radiat.* **2005**, *12*, 537–541. [CrossRef]

31. Rehr, J.J.; Leon, J.; Zabinsky, S.I.; Albers, R.C. Theoretical X-Ray absorption fine-structure standards. *J. Am. Chem. Soc.* **1991**, *113*, 5135. [CrossRef]

32. Ahmad, Z.U.; Chao, B.; Konggidinata, M.I. Molecular simulation and experimental validation of resorcinol adsorption on Ordered Mesoporous Carbon (OMC). *J. Hazard. Mater.* **2018**, *354*, 258–265. [CrossRef] [PubMed]

33. Perdew, J.P.; Wang, Y. Accurate and simple analytic representation of the electron-gas correlation energy. *Phys. Rev. B.* **1992**, *45*, 13244–13249. [CrossRef] [PubMed]

34. Simunek, J.; Genuchten MT, V.; Sejna, M. The HYDRUS-1D software package for simulating the one-dimensional movement of water, heat, and multiple solutes in variably-saturated media. *Univ. Calif.-Riverside Res. Rep.* **2005**, *3*, 1–240.

35. Patterson, A.L. The Scherrer Formula for X-Ray particle size determination. *Phys. Rev.* **1939**, *56*, 978–982. [CrossRef]

36. Liu, Y.; Tan, J.; Owens, G.; Chen, Z. Removal of Cr (VI) from aqueous solutions via reduction and absorption by green synthesized iron nanoparticles. *J. Clean. Prod.* **2018**, *176*, 929–936.

37. Luxton, T.P.; Eick, M.J.; Rimstidt, D.J. The role of silicate in the adsorption/desorption of Arsenite on goethite. *Chem. Geo.* **2008**, *252*, 125–135. [CrossRef]

38. Rahimi, S.; Moattari, R.M.; Rajabi, L.; Derakhshan, A.A.; Keyhani, M. Iron oxide/hydroxide (α, γ-FeOOH) nanoparticles as high potential adsorbents for lead removal from polluted aquatic media. *J. Ind. Eng. Chem.* **2015**, *23*, 33–43. [CrossRef]

39. Sk, A.; Sme, B. Adsorption of chromium (VI) onto natural mesoporous goethite: Effect of calcination temperature. *Groundw. Sustain. Dev.* **2019**, *9*, 100250.

40. Poudel, M.B. Novel insight into the adsorption of Cr (VI) and Pb (II) ions by MOF derived Co-Al layered double hydroxide @hematite nanorods on 3D porous carbon nanofiber network. *Chem. Eng. J.* **2021**, *417*, 129312. [CrossRef]

41. Varanda, L.C.; Morales, M.P.; Jafelicci Jr, M.; Serna, C.J. Monodispersed spindle-type goethite nanoparticles from Fe III solutions. *J. Mater. Chem.* **2002**, *12*, 3649–3653. [CrossRef]

42. Bekkar, D.; Meftah, Y.; Benhaoua, B.; Rahal, A.; Benhaoua, A.; Hamzaoui, A.H. Synthesis, Characterization, and antibacterial activity of cobalt doped (α-Fe$_2$O$_3$) thin films. *J. Optoelectron. Biome.* **2020**, *12*, 33–42.

43. Oulego, P.; Villa-García, M.; Laca, A.; Diaz, M. The effect of the synthetic route on the structural, textural, morphological and catalytic properties of iron (III) oxides and oxyhydroxides. *Dalton. Trans.* **2016**, *45*, 9446–9459. [CrossRef] [PubMed]

44. Sangwichien, C.; Aranovich, G.L.; Donohue, M.D. Density functional theory predictions of adsorption isotherms with hysteresis loops. *Colloid. Surf. A. Phys. Eng. Aspect.* **2002**, *206*, 313–320. [CrossRef]

45. Nemr, A.E.; Khaled, A.; Abdelwahab, O.; El-Sikail, A. Treatment of wastewater containing toxic chromium using new activated carbon developed from date palm seed. *J. Hazard. Mater.* **2008**, *152*, 263–275. [CrossRef] [PubMed]

46. Yuan, X.; Wang, Y.; Wang, J.; Zhou, C.; Tang, Q.; Rao, X. Calcined graphene/MgAl-layered double hydroxides for enhanced Cr (VI) removal. *Chem. Eng. J.* **2013**, *221*, 204–213. [CrossRef]

47. Hyder AH, M.G.; Begum, S.A.; Egiebor, N.O. Adsorption isotherm and kinetic studies of hexavalent chromium removal from aqueous solution onto bone char. *J. Environ. Chem. Eng.* **2015**, *3*, 1329–1336. [CrossRef]

48. Qiu, B.; Xu, C.; Sun, D.; Wang, Q.; Gu, H.; Zhang, X.; Weeks, B.; Hopper, J. Polyaniline coating with various substrates for hexavalent chromium removal. *Appl. Surf.* **2015**, *334*, 7–14. [CrossRef]

49. Zhao, Y.; Yang, S.; Ding, D.; Chen, J.; Zhang, Z. Effective adsorption of Cr (VI) from aqueous solution using natural Akadama clay. *J. Colloid. Interface. Sci.* **2013**, *395*, 198–204. [CrossRef]

50. Adegoke, H.I.; Amooadekola, F.; Fatoki, O.S.; Ximba, B.J. Adsorption of Cr (VI) on synthetic hematite (α-Fe$_2$O$_3$) nanoparticles of different morphologies. *Korean. J. Chem. Eng.* **2014**, *31*, 142–154. [CrossRef]

51. Omar, A.; Charlotte, H.; Mohammed, A.; Allal, L.B.; Marmier, N. Sorption of Cr (VI) onto natural iron and aluminum (oxy)hydroxides: Effects of pH, ionic strength and initial concentration. *J. Hazard. Mater.* **2010**, *174*, 616–622.

52. Picazo-Rodríguez, N.G.; Carrillo-Pedroza, F.R.; Soria-Aguilar, M.J. Use of thermally modified jarosite for the removal of hexavalent chromium by adsorption. *Crystals* **2022**, *12*, 80. [CrossRef]

53. Lagergren, S. About the theory of so-called adsorption of solution substances. *K. Sven. Vetensk. Handl. Band* **1898**, *24*, 1–39.

54. Ho, Y.S.; McKay, G. Pseudo-second order model for sorption processes. *Process. Biochem.* **1999**, *34*, 451–465. [CrossRef]

55. Fendorf, S.; Eick, M.J.; Grossl, P.; Sparks, D.L. Arsenate and chromate retention mechanisms on goethite. 1. Surface structure. *Environ. Sci. Technol.* **1997**, *31*, 315–320. [CrossRef]

56. Pandya, K.I. Multiple-scattering effects in X-ray-absorption fine structure: Chromium in a tetrahedral configuration. *Phys. Rev. B* **1994**, *50*, 15509–15515. [CrossRef]

57. Johnston, C.P.; Chrysochoou, M. Mechanisms of chromate adsorption on hematite. *Geochimica Cosmochimica Acta.* **2014**, *138*, 146–157. [CrossRef]

58. Tang, S.; Ke, Y.; Lo, I. Column study of Cr (VI) removal by cationic hydrogel for in-situ remediation of contaminated groundwater and soil. *J. Contam. Hydrol.* **2011**, *125*, 39–46. [CrossRef]

59. Li, Z. Chromate transport through surfactant-modified zeolite columns. *Groundw. Monit. Remed.* **2010**, *26*, 117–124. [CrossRef]

60. Lv, G.; Li, Z.; Jiang, W.T.; Ackley, C.; Demarco, N. Removal of Cr (VI) from water using Fe (II)-modified natural zeolite. *Chem. Eng. Res. Design.* **2014**, *92*, 384–390. [CrossRef]

61. Du, G.; Li, Z.; Liao, L.; Hanson, R.; Leick, S.; Hoeppner, N.; Jiang, W.T. Cr (VI) retention and transport through Fe (III)-coated natural zeolite. *J. Hazard. Mater.* **2012**, *221*, 118–123. [CrossRef] [PubMed]